



# Microelectromechanical Systems for Nanomechanical Testing: Electrostatic Actuation and Capacitive Sensing for High-Strain-Rate Testing

C. Li<sup>1</sup> · D. Zhang<sup>1,2</sup> · G. Cheng<sup>1</sup> · Y. Zhu<sup>1</sup>

Received: 15 November 2018 / Accepted: 19 November 2019 / Published online: 9 December 2019

© Society for Experimental Mechanics 2019

## Abstract

There have been relatively few studies on mechanical properties of nanomaterials under high strain rates, mainly due to the lack of capable nanomechanical testing devices. Here we present a new on-chip microelectromechanical system (MEMS) for high strain-rate nanomechanical testing. The MEMS device consists of an electrostatic comb drive actuator, two capacitive displacement sensors and a load cell. The dynamic responses of the device in air and in vacuum are systematically modeled under both alternating and ramp forces. Two methods, capacitive readout and high-speed imaging, are used to measure the dynamic displacements, which agree well with the modeling results. While we demonstrate the maximum constant strain rate over  $200\text{ s}^{-1}$  under ramp force, it is interesting to find that the capacitive readout used in this work can only measure strain rate up to  $22\text{ s}^{-1}$  due to its limit in bandwidth. To demonstrate the utility of this new device, gold nanowires are tested at strain rates of  $10^{-5}$  and  $10\text{ s}^{-1}$  inside a scanning electron microscope. Increasing strain rate is found to yield higher yield strength and larger ductility.

**Keywords** Nanomechanics · MEMS · High strain rate

## Introduction

With rapid advances in nanotechnology in the past decades, a plethora of nanomaterials with outstanding material properties have been developed and a number of nanomaterial-enabled applications have emerged. One-dimensional (1D) nanomaterials are among the most important building blocks for these nano-enabled applications. For example, metal nanowires have been widely used in flexible and stretchable electronics applications such as flexible transparent electrodes, wearable sensors, soft actuators and deformable antennas [1–3]. The operation and reliability of these device applications call for a thorough understanding of mechanical behaviors of nanowires.

Mechanical behaviors of nanowires have been extensively investigated through atomistic simulations. Experimental investigations have emerged recently as a result of advances in novel experimental methods [4–6]. Nanowires have been found to exhibit ultrahigh strength [7–9], size-dependent elasticity [10–12], and dislocation nucleation from free surfaces [13, 14]. A number of interesting rate- (or time-) dependent phenomena have been reported recently, such as stress relaxation and creep [15, 16], recoverable plasticity [15, 17], Bauschinger effect [15, 17], brittle-to-ductile transition [18, 19], and anelasticity [20]. However, most of the nanomechanical testing was conducted quasi-statically; high strain-rate testing of nanowires remains an area largely unexplored. It is in great need to conduct high strain-rate testing since nanowires especially metal nanowires can behave differently at high strain rates [14, 19, 21], which is of relevance to applications where these 1D nanomaterials are subject to high-rate loadings.

It is, however, challenging to conduct high strain-rate nanomechanical testing. Microelectromechanical system (MEMS) has been widely used for nanomechanical testing [22–25] and might provide a solution to the high strain-rate testing. Naraghi et al. [26, 27] reported testing of polymer nanofibers

✉ Y. Zhu  
yong\_zhu@ncsu.edu

<sup>1</sup> Department of Mechanical and Aerospace Engineering, North Carolina State University, Raleigh, NC 27695, USA

<sup>2</sup> College of Mechanical and Electrical Engineering, Zhengzhou University of Light Industry, Zhengzhou 450002, Henan, China

with strain rate up to  $200\text{ s}^{-1}$  using a MEMS-based load sensor and an external piezoelectric actuator. The external actuator provided the fast actuation, while force and displacement were measured from high-speed optical images using digital image correlation (DIC). However, this off-chip actuation method adds complexity for in-situ scanning or transmission electron microscope (SEM/TEM) testing and might be challenging in handling smaller samples such as nanowires (with diameters generally less than 100 nm).

As for the on-chip method, the strain rate attained so far has been quite limited, mostly less than  $0.1\text{ s}^{-1}$  [14, 21]. Ramachandramoorthy et al. [19] reported high strain rate tensile testing of silver nanowires (up to  $2\text{ s}^{-1}$ ) using an on-chip MEMS thermal actuator. While the capacitive load sensor responded quickly, the thermal actuator limited the actuation speed due to the relatively slow heat transfer process. Nevertheless  $2\text{ s}^{-1}$  is the largest strain rate that has been reported for tensile testing of nanowires so far. For metallic nanowires surface dislocation nucleation is the dominant deformation mechanism, which has been recently shown to exhibit pronounced temperature and strain rate dependence [13, 14]. It is of important relevance to experimentally investigate how higher strain rate can impact dislocation nucleation and interactions, hence mechanical behavior of nanowires. A potential solution is to employ other types of MEMS actuators that can respond faster.

In this paper, we systematically investigated the dynamic response of a MEMS-based nanomechanical testing device with an electrostatic actuator and a capacitive sensor in air and inside SEM (near vacuum environment). The goal is to explore the maximum actuation speed and maximum strain rate attainable. The structure and operating principle of the device is first described. Analytical model is derived to thoroughly investigate the dynamic response to AC actuation force and ramp force. The dynamic responses are then measured in air and in vacuum, which compared well with the modeling results. The maximum strain rate that the device can attain is discussed based on the modeling and experiment results. We demonstrated that this device is able to achieve constant strain rate above  $200\text{ s}^{-1}$  under ramp force; however, the capacitive readout can only measure strain rate up to  $22\text{ s}^{-1}$  due to its limited bandwidth. Finally, two gold nanowires are tested at strain rates of  $10^{-5}\text{ s}^{-1}$  and  $10\text{ s}^{-1}$  in SEM to demonstrate the capability of the device for high strain-rate nanomechanical testing.

## Device Description

The MEMS devices were fabricated at MEMSCAP (Durham, NC) using the Silicon-on-Insulator Multi-User MEMS Process. Figure 1 shows a SEM image, schematic and lumped mechanical model of the MEMS device. The device consists

of a comb-drive actuator, two displacement sensors (A and B) and a folded beam load cell (sensor). The central shuttle of the device is supported by four beams. A specimen is to be placed across the gap between Sensor B and the fixed anchor. Elongation of the specimen is simply determined by the displacement of Sensor B. If the damping force in Sensor B is negligible (e.g., under quasi-static loading), then force in the specimen is equal to elongation of the load cell (displacement difference between Sensors A and B) multiplied by the stiffness of the load cell because forces in the specimen and the load cell are equal (two springs connected in series). The dynamic force measurement will be discussed later. Stress and strain of the specimen can be calculated given the specimen's gauge length and cross-sectional area.

The configuration used here, similar to that of Tsuchiya et al. [28], is different from most MEMS-based nanomechanical testing devices where a specimen is placed between the actuator and the load cell. The current configuration eliminates the specimen rigid body motion due to the load cell displacement, which makes tracking the specimen deformation easier during in-situ testing. In addition, with this configuration, strain rate of the specimen can simply be defined by

$$\dot{\varepsilon} = \frac{1}{l_0} \frac{\partial d_B}{\partial t} \quad (1)$$

where  $d_B$  is the displacement of Sensor B,  $\frac{\partial d_B}{\partial t}$  is the velocity of Sensor B, and  $l_0$  is the gauge length of the specimen.

The actuator used in this work is an electrostatic comb-drive actuator. Compared to other types of actuators such as electrothermal actuator [29, 30], comb-drive actuator can provide a constant force under a constant actuation voltage regardless of the travel distance and with no heating effect. The actuation force is proportional to the actuation voltage squared as given by [31].

$$F_A = N_A \varepsilon \left( \frac{h}{g} \right) V^2 \quad (2)$$

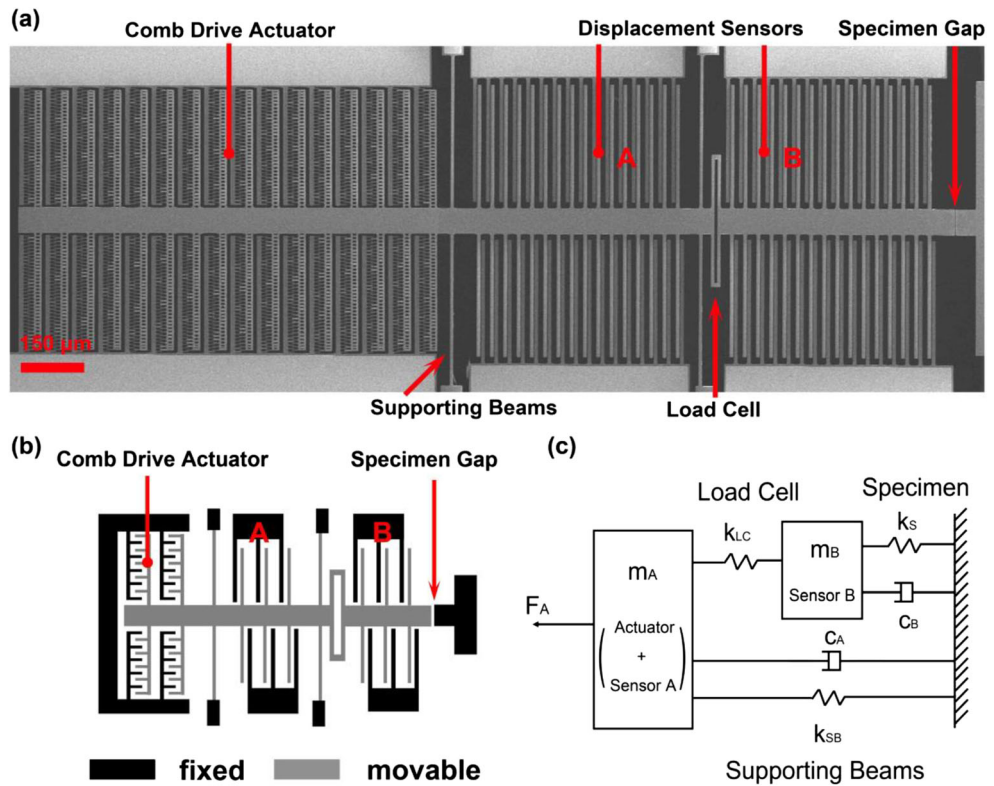
where  $N_A$  is the number of pairs of comb fingers,  $\varepsilon$  is the permittivity,  $h$  is the thickness of the MEMS structure,  $g$  is the lateral gap between comb fingers, and  $V$  is the actuation voltage.

Both sensors (A and B) are the differential capacitive sensors, which can provide a quasi-linear relationship [32, 33] between displacement  $d$  and capacitance difference  $\Delta C$ , viz.,

$$\Delta C = N_S \varepsilon A \left( \frac{1}{g_1 - d} - \frac{1}{g_1 + d} \right) \approx 2N_S \varepsilon A \frac{d}{g_1} \quad (3)$$

where  $N_S$  is the number of pairs of parallel plates,  $A$  is the overlapping area of two adjacent plates, and  $g_1$  is the initial gap between the fixed plate and the closer movable plate.

**Fig. 1** (a) SEM micrograph of the fabricated device. (b) Schematic of MEMS device configuration. (c) Device lumped mechanical model



## Modeling

Based on the lumped mechanical model shown in Fig. 1c, equations of motion of the device can be written as

$$m_A \ddot{d}_A + c_A \dot{d}_A + k_{SB} \dot{d}_A + k_{LC}(d_A - d_B) = F_A \quad (4)$$

$$m_B \ddot{d}_B + c_B \dot{d}_B + k_S \dot{d}_B - k_{LC}(d_A - d_B) = 0 \quad (5)$$

where  $m_A$  is the total mass of the moving portion of Sensor A and the actuator,  $m_B$  is the mass of the moving portion of Sensor B,  $d_A$  and  $d_B$  are the displacements of  $m_A$  and  $m_B$ , respectively,  $k_{SB}$ ,  $k_{LC}$  and  $k_S$  are the stiffness of the supporting beams, load cell and specimen, respectively, and  $c_A$  and  $c_B$  are the damping coefficients with respect to  $m_A$  and  $m_B$ , respectively.

### Dynamic Response under AC Actuation Force: Vacuum and Air

For a linear system, dynamic response under AC actuation force (or frequency response) of the system can be characterized by its transfer function. In order to find out transfer function of this MEMS device, a state-space model was constructed based on the aforementioned equations of motion, viz.,

$$\dot{\mathbf{X}} = A\mathbf{X} + Bu \quad (6)$$

$$y = CX \quad (7)$$

where state vector  $\mathbf{X} = \begin{bmatrix} d_B \\ \dot{d}_B \\ d_A \\ \dot{d}_A \end{bmatrix}$ ,

$$\text{state matrix } A = \begin{bmatrix} 0 & 1 & 0 & 0 \\ -\frac{k_{LC} + k_S}{m_B} & -\frac{c_B}{m_B} & \frac{k_{LC}}{m_B} & 0 \\ 0 & 0 & 0 & 1 \\ \frac{k_{LC}}{m_A} & 0 & -\frac{k_{LC} + k_{SB}}{m_A} & -\frac{c_A}{m_A} \end{bmatrix},$$

$$\text{input matrix } B = \begin{bmatrix} 0 \\ 0 \\ 0 \\ 1 \end{bmatrix}, \text{ and input } u = F_A. \text{ Here only the}$$

displacement of Sensor B is chosen as the output since it is directly related to the specimen elongation, hence output  $y = d_B$  and output matrix  $C = [1 \ 0 \ 0 \ 0]$ . The system transfer function is then written as

$$G(s) = C(sI - A)^{-1}B = \frac{k_{LC}}{m_A m_B s^4 + (c_A m_B + c_B m_A)s^3 + (c_A c_B + k_{SB} m_B + k_S m_A + k_{LC}(m_A + m_B))s^2 + c_B(k_{LC} + k_{SB})s + c_A(k_{LC} + k_S)s + k_S k_{SB} + k_{LC} k_S + k_{LC} k_{SB}} \quad (8)$$

where  $s = j\omega$  with  $\omega$  as the angular frequency, and  $I$  is the identity matrix. In Eq. (8),  $m_A = 1.68 \times 10^{-8}$  kg and  $m_B = 5.99 \times 10^{-9}$  kg,  $k_{SB} = 107$  N/m, and  $k_{LC} = 850$  N/m. Supporting beam stiffness and load cell stiffness were estimated by finite element analysis based on the measured dimensions using SEM.  $k_S$  is zero when there is no specimen mounted.

In vacuum, the damping coefficients  $c_A$  and  $c_B$  are assumed to be zero, neglecting the intrinsic damping. With all the system parameters known, transfer function of the device in vacuum can be calculated using Eq. (8). Figure 2 plots bode magnitude plot of the device, which characterizes the relationship between the angular frequency  $\omega$  of the input force  $F_A$  and the magnitude of the output displacement  $d_B$  with respect to displacement at  $\omega = 0$ . Since the system has two degrees of freedom, two peaks can be found corresponding to two undamped frequencies at resonance,  $\omega_1 = 72,193$  rad/s and  $\omega_2 = 440,997$  rad/s. Note that without damping, the magnitude approaches infinity at the natural frequencies.

In air, the damping effect needs to be considered. The damping coefficients  $c_A$  and  $c_B$  must be known in order to characterize the dynamic response of the device under AC actuation force. The two natural frequencies in air,  $\omega_3$  and  $\omega_4$ , are expected to be smaller than their counterparts in vacuum if the device is underdamped in air. The damping coefficients of the device in air will be determined through experiments as described in Section 4.2 and theoretical calculation in Section 6.2.

### Dynamic Response under Ramp Actuation Force: Vacuum and Air

To attain a constant strain rate in the specimen, i.e., constant velocity of Sensor B, a ramp force  $F_A = \xi t$  is chosen as the input to the device, where the loading rate  $\xi$  is a constant.

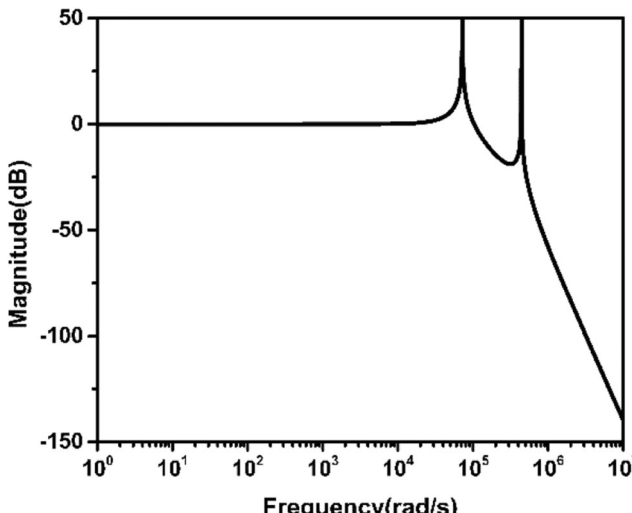


**Fig. 2** Bode magnitude plot of the device in vacuum

In vacuum, the damping coefficients are zero, hence the device model is simplified to a two-coupled-mass-spring system [34]. The system transient output  $d_B(t)$  has the following form

$$d_B(t) = \frac{\xi t}{k_{SB}} - a_1 \xi \sin(2\pi f_1 t) + a_2 \xi \sin(2\pi f_2 t) \quad (9)$$

where  $a_1$  and  $a_2$  are constants that can be calculated with the known system parameters (e.g.,  $m_A$ ,  $m_B$ ,  $k_{SB}$ ,  $k_{LC}$ ) (both independent of  $\xi$ ), and  $f_1$  and  $f_2$  are the two natural frequencies of the system in vacuum as identified in Section 3.1 ( $\omega = 2\pi f$ ).  $\frac{\xi t}{k_{SB}}$  is defined as the nominal loading velocity. The output form of this two-coupled-mass-spring system is similar to that of a single-mass-spring system (see Appendix), but has to be solved numerically. The analytical solution of the single-mass-spring system can shed some light on the two-coupled-mass-spring system (i.e. the present device). The same goes for the single-mass-spring-damper system (see below). As shown in Eq. (9),  $d_B(t)$  is the superposition of a linear displacement  $\frac{\xi t}{k_{SB}}$  and two sinusoidal displacements, which is schematically shown in Fig. 3a. The linear displacement is the ideal displacement of Sensor B to achieve a constant strain rate in the specimen. The two sinusoidal displacements can be considered as deviation from the ideal linear displacement. Magnitude of the deviation is proportional to  $\xi$ . When  $\xi$  is small, the deviation is negligible, which is the case for quasi-static loading. However, this does not hold when  $\xi$  is large.

In air, considering the damping effect, the device model becomes a two-coupled-mass-spring-damper system. The system transient output  $d_B(t)$  has the following form

$$d_B(t) = \frac{\xi t}{k_{SB}} - a_3 \xi - a_4 \xi e^{-a_5 t} \sin(2\pi f_3 t + a_6) + a_7 \xi e^{-a_8 t} \sin(2\pi f_4 t + a_9) \quad (10)$$

where  $a_3$  to  $a_9$  are constants ( $a_5$  and  $a_8$  are positive) that can be calculated with the known system parameters (e.g.,  $m_A$ ,  $m_B$ ,  $k_{SB}$ ,  $k_{LC}$ ,  $c_A$ ,  $c_B$ ) (all independent of  $s$ ), and  $f_3$  and  $f_4$  are the two natural frequencies of the system in air. The form is again similar to that of a single-mass-spring-damper system (see Appendix). Displacement  $d_B$  contains a linear term  $\frac{\xi t}{k_{SB}}$  (the ideal displacement), a constant offset term  $a_3 \xi$ , and two attenuated sinusoidal terms. Here the sum of the last three terms is the deviation with a magnitude also proportional to  $\xi$ . Figure 3b shows schematically the displacement  $d_B(t)$  in this case.

## Experiments

Dynamic responses of the device were measured experimentally under AC actuation and ramp actuation. Two methods

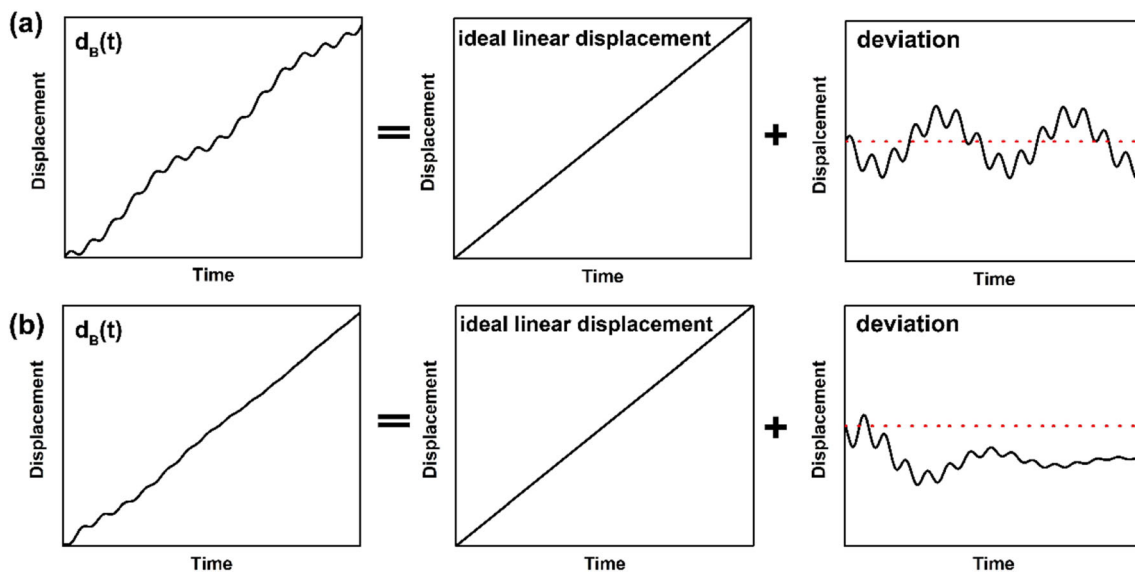


**Fig. 3** Illustration of Sensor B displacement when the device is actuated by a linear ramp force (a) in vacuum, (b) in air. For both cases, Sensor B displacement is the superposition of an ideal linear displacement (constant velocity and correspondingly constant strain rate) and deviation. Horizontal dashed line marks zero deviation

were employed to measure displacement – optical imaging and capacitance readout. The responses in air, under both AC actuation and ramp actuation, were measured by the optical imaging, while the response in vacuum under ramp actuation was measured by the capacitive readout. The purpose of the response under AC actuation is to validate the theory in Section 3.1 and obtain damping coefficients.

To image the displacement under dynamic testing, a high-speed camera (Phantom v4.3 with maximum frame rate 95,000 fps) was integrated to a Nikon LV150N optical microscope (100 $\times$  objective, N.A. = 0.8), as shown in Fig. 4. A light source (SOLA SE II 365) was used to provide strong white light needed for the high-speed imaging.

The recorded images were processed using an image correlation method to obtain displacement. The method used here is based on the shift theorem of discrete Fourier transformation (DFT) [35]. A series of optical images were taken to record the positions of Sensor B at different moments (Fig. 5a). Then the images were cropped to the same region of interest – some parallel beams connected to the shuttle, which is a periodic pattern as marked by the red rectangle in Fig. 5a. For each cropped image, the gray value of pixels in each column was averaged to produce a 1D periodic pixel intensity profile (Fig. 5b), which was then analyzed using DFT (Fig. 5c). Since displacement in spatial domain (Fig. 5b) corresponds to phase shift in frequency domain (Fig. 5c), the phase of the fundamental frequency, which is the spatial frequency of the periodic pattern, was recorded for each image; phase shift between images was then converted back to the spatial domain to calculate the displacement. To remove common motion induced noises such as vibration, a fixed periodic structure can be chosen as the region of interest

(the green rectangle in Fig. 5a) to serve as a reference, whose displacement can be subtracted from the displacement of the moving structure.

When compared with other displacement measurement techniques based directly on image processing, such as the commonly used DIC, this single frequency-based DFT method is less affected by image noises since only phase of the fundamental frequency is used to retrieve displacement. It has been demonstrated that even blurring and defocusing of

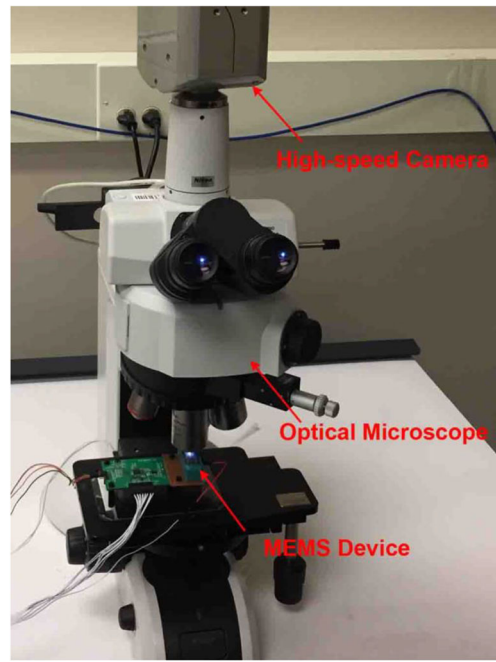


**Fig. 4** Experiment setup to measure the displacement including a high-speed camera and an optical microscope

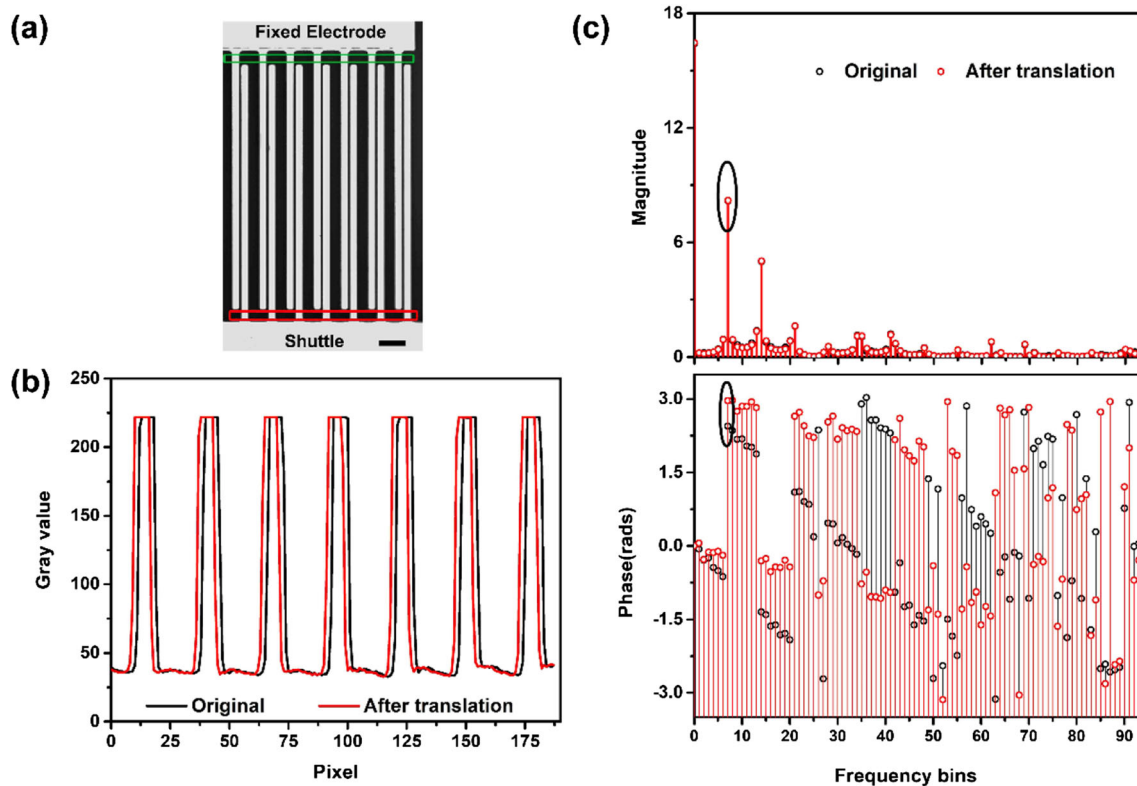


**Fig. 5** (a) One frame of the high-speed image. Scale bar 30  $\mu\text{m}$ . (b) 1D line intensity profile of the periodic pattern in the region of interest before and after translation. (c) DFT of the line intensity profile before and after translation (upper is magnitude plot and lower is phase plot). Fundamental frequency corresponding to the spatial frequency of the periodic patterns is circled out. Phase shift of the fundamental frequency is used to retrieve the translational displacement

optical images have little effect on the accuracy of displacement measurement using this method [36, 37] because blurring and defocusing act as low-pass filters; hence only the higher order harmonics are degraded, leaving the fundamental frequency mostly untouched. This feature makes this method particularly suitable for dynamic displacement measurement since the device is moving during exposure, leading to certain degree of blurring. One limitation of this method originates from the nature of the high-speed camera used in this work – high frame rate is accompanied by reduced field of view. With the small field of view, the uncertainty in measured displacement increases because the less the repeated patterns are captured the worse the measurement accuracy is [35]. Another limitation of this method is that it is not suitable for measure displacement inside electron microscopes.

The other method is using a capacitive readout circuit to measure displacement. There is a linear relationship between displacement and capacitance difference in the sensors (Eq. (3)). A commercially available capacitive readout AT1006 (ACT-LSI, Japan) [28] was used, which converts the differential capacitance linearly into an output voltage. Figure 6a shows the function blocks of AT1006 and its connection to the MEMS chip; more specifically, channels X and Y are connected to Sensors A and B, respectively. Figure 6b shows the MEMS chip integrated with the readout. Before the

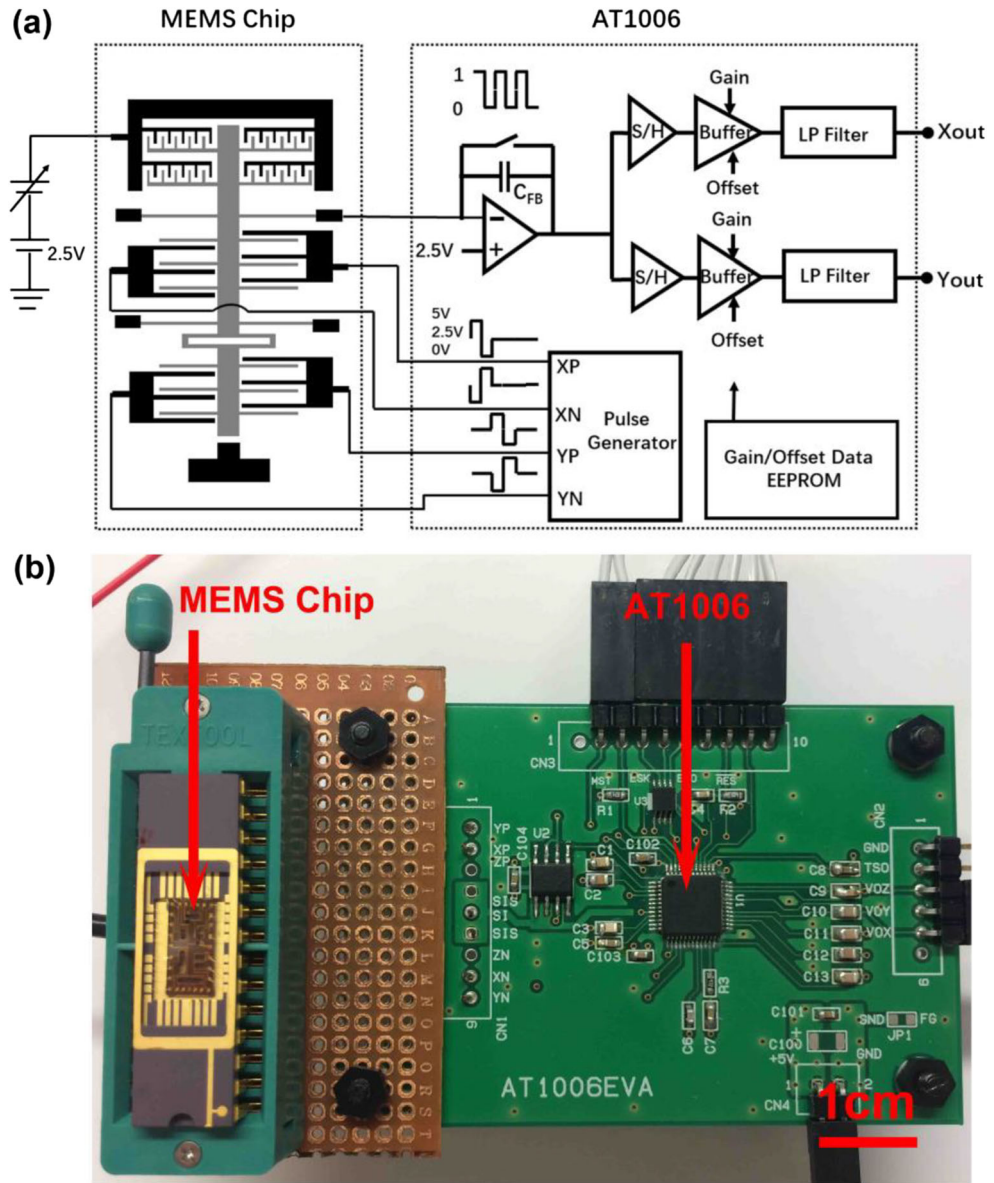
readout can be used to measure displacement, the relationship between displacement and AT1006 output voltage was calibrated. The calibration result is linear as shown in Fig. 7, in good agreement with Eq. (3). A NI DAQ (USB-6211 with the maximum sample rate of 250 kHz) was used to record the voltage reading from AT1006. Compared with the optical method, this method has two major advantages: 1) it can be used both in air and in vacuum, and 2) it can measure displacements of both sensors A and B at the same time, with which force on the specimen can be calculated. Unfortunately the bandwidth of this readout circuit is relatively low (~1100 Hz), to be discussed later, which prevents this method from measuring high-frequency signals.

## Results

### AC Response

To study dynamic response of the device under AC actuation force, AC voltage  $V_{pp} = 30$  V at different frequencies was applied to the actuator using a function generator (Agilent 33250A). Amplitude of the output displacement  $d_B$  was measured as a function of the actuation force frequency. Note that there is a factor of 2 between the actuation voltage frequency

**Fig. 6** (a) Functional block diagram of the capacitive readout AT1006 and its connection with the MEMS device. (b) Image of the MEMS device and the capacitive readout



and the resulting actuation force (or displacement) frequency because of the squared relationship as shown in Eq. (2).

Since only the electronic method can be used to measure displacement in vacuum but its relatively low bandwidth makes it unable to detect the resonance peaks as predicted in Section 3.1, measurements were focused on the dynamic response under AC actuation force in air using the optical method. For the optical method, in order to improve the measurement accuracy, a larger field of view and more periodic beams are preferred, as discussed in Section 4.1. Hence to accurately measure displacement at high frequency, a low frame rate associated with large field of view was used. This way “aliasing” can occur, so the measured frequency is not the actual displacement oscillation frequency. But amplitude of the oscillation can still be retrieved if the frame rate and exposure time are set properly. For example, a low frame rate of

100 fps with short exposure time can be used for displacement oscillation of 2002 Hz (the actuation voltage frequency is purposely set as 1001 Hz). In this case, an image is taken every 20.02 displacement oscillation cycles. These images record different phases of the oscillation waveform, from which the oscillation amplitude can be retrieved. Figure 8a shows the optically measured displacement of sensor B using the “aliasing” method. The displacement amplitude as a function of frequency was normalized by the amplitude at 1 Hz, as shown in Fig. 8b. Only the lower natural frequency in air, 10.6 kHz, was measured, which is a little smaller than the counterpart in vacuum, 11.5 kHz, as calculated by the model in Section 3.1.

This measured relationship was fitted using magnitude of normalized transfer function  $\left| \frac{G(j2\pi f)}{G(2\pi)} \right|$ , where the denominator

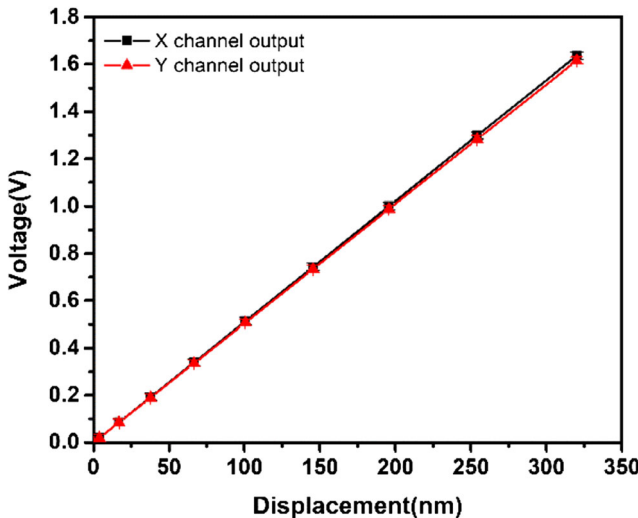


**Fig. 7** Calibrated relationship between AT1006 output voltages and measured displacements of sensor A and B

accounts for the normalization at 1 Hz. By fitting the curve in Fig. 8b, damping coefficients in air  $c_A = 3.09 \times 10^{-4}$  kg/s and  $c_B = 2.83 \times 10^{-4}$  kg/s were obtained. The damping coefficients can be used to calculate the second natural frequency  $f_4$  and the device displacement in air under ramp actuation force in the next section. To summarize,  $f_1$  to  $f_4$  are 11.5, 70.2, 10.6, and 70.0 kHz, respectively.

### Ramp Response: Vacuum and Air

In this section, the dynamic responses under ramp actuation force in both vacuum and air were first predicted. Then a ramp actuation force with gradually increasing loading velocity was applied to the device in both vacuum and air while Sensor B displacement was measured.

To provide a linear ramp actuation force, an actuation voltage profile  $V(t) = \lambda t^{0.5}$  was applied to the comb-drive actuator, where  $\lambda$  is a function of the loading rate  $\xi$  via Eq. (2) and  $t$  is

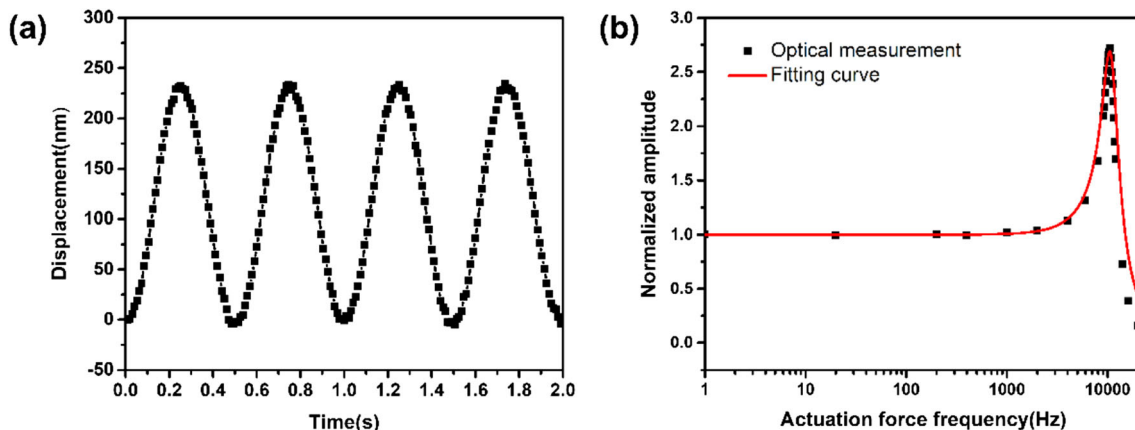


**Fig. 8** (a) Optically measured displacement at frequency of 2002 Hz (the frame rate used is 100 fps). (b) Relationship between actuation force frequency and normalized displacement amplitude measured using the optical method. The optical measurement result was fitted, from which the damping coefficients in air were obtained

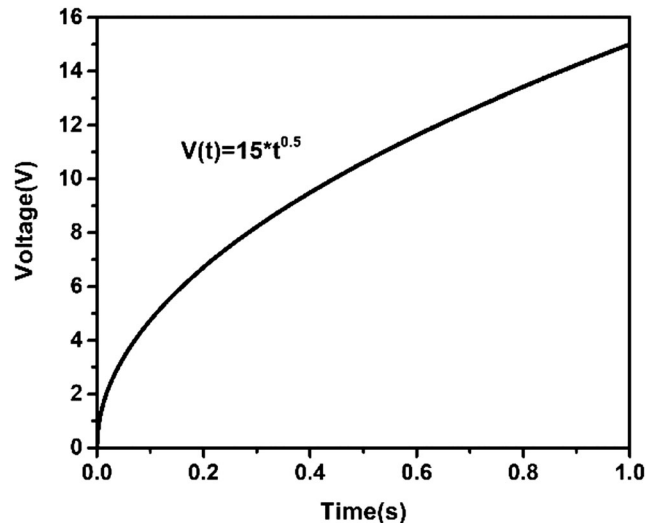


**Fig. 9** Voltage profile to achieve the linearly ramp actuation force (loading time of 1 s)

the loading time. The larger  $\lambda$ , the smaller the loading time it takes to reach the desired actuation voltage. As an example, Fig. 9 shows the actuation voltage profile up to 15 V with the loading time of 1 s. In this case  $\lambda = 15 \text{ V/s}^{0.5}$  in the actuation voltage profile, the loading rate  $\xi = 24.2 \mu\text{N/s}$ , and the loading velocity is 226 nm/s. Figures 10 and 11 show the displacement as a function of the loading time in both vacuum and air, as calculated by Eqs. 9 and 10, respectively. A series of tests were conducted, during which the actuation voltage was increased from 0 to 15 V while the loading time was decreased to increase the loading velocity.

The vacuum experiments were conducted inside a SEM (FEI Quanta 3D FEG). Of course the vacuum was not absolute. The displacement  $d_B$  was measured using the capacitive readout and compared with the modeling result according to Eq. (9). Figure 10 shows the displacement vs. time when the loading velocity was 226 nm/s, 45.2  $\mu\text{m/s}$ , and 226  $\mu\text{m/s}$  (corresponding loading time of 1 s, 5 ms, and 1 ms,

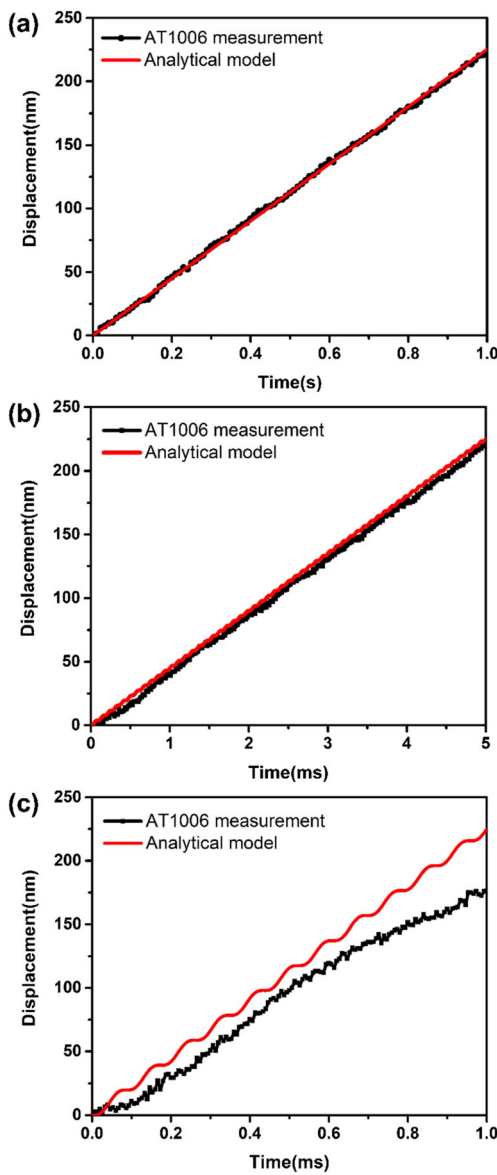


**Fig. 10** Comparison of displacements from the dynamics and measured using AT1006 in vacuum when loading time is (a) 1 s, (b) 5 ms, and (c) 1 ms.

respectively). When the loading velocity was 226 nm/s (Fig. 10a), the measured and modeled displacements agreed very well, both increasing linearly with time. When the loading velocity was increased to 45.2  $\mu\text{m}/\text{s}$  (Fig. 10b), the measured displacement started to show a small lag compared to the modeled displacement (about 2% smaller) due to the limitation in bandwidth. The sensor B velocity 45.2  $\mu\text{m}/\text{s}$  in this case was thus considered to be the upper bound that can be measured using the capacitive readout AT1006. When the loading velocity was increased to 226  $\mu\text{m}/\text{s}$  (Fig. 10c), the measurement was further lagged, again due to the limitation in bandwidth. The sinusoidal deviation appears to have only one frequency rather than two as predicted by Eq. (9). This is because the amplitude of the larger natural frequency is

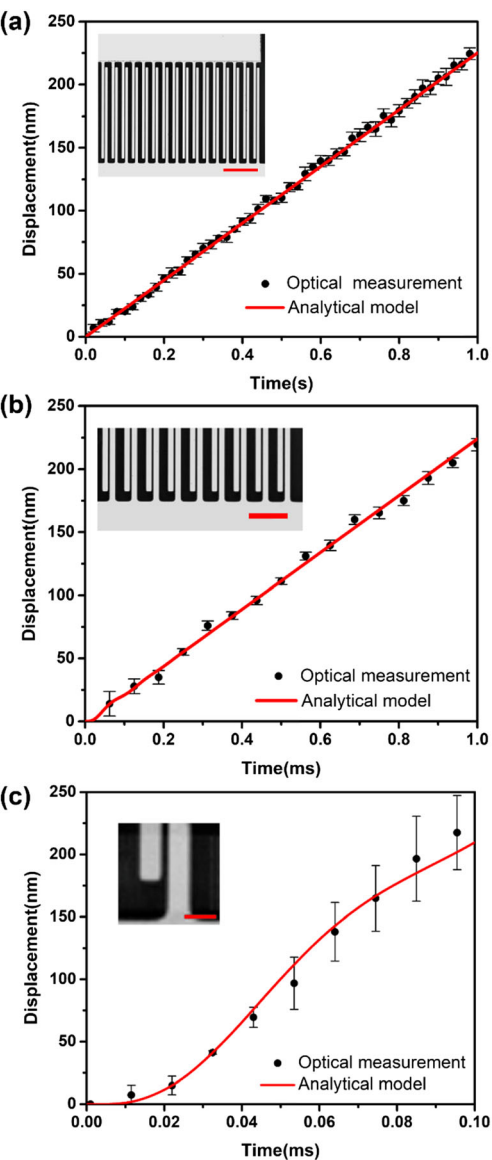


**Fig. 11** Comparison of displacements from the dynamics model and measured optically in air when loading time is (a) 1 s, (b) 1 ms, and (c) 0.1 ms. The frame rates are 50 fps, 16,000 fps, 95,000 fps, respectively. Insets are the corresponding images. Scale bars are 100  $\mu\text{m}$ , 50  $\mu\text{m}$  and 10  $\mu\text{m}$ , respectively. A higher frame rate is associated with a smaller field of view. In (c), the field of view reaches the lower limit, where the field of view is about 35  $\mu\text{m}$  by 35  $\mu\text{m}$

negligible compared to that of the lower natural frequency. For example, when the loading velocity is 226  $\mu\text{m}/\text{s}$ , the calculated amplitude is 3.2 nm for the lower natural frequency and 0.01 nm for the larger natural frequency. Of note is that even the lower natural frequency predicted is 11.5 kHz, much larger than the capacitive readout bandwidth.

The dynamic response under the ramp actuation force was also studied in air. The optical method was used to measure the displacement  $d_B$ . Figure 11 shows the experimentally measured and analytically predicted displacement  $d_B$  with the loading velocity of 226 nm/s, 226  $\mu\text{m}/\text{s}$ , and 2.26 mm/s

(corresponding loading time of 1 s, 1 ms, and 0.1 ms, respectively). The high-speed camera frame rate used was 50, 16,000, and 95,000 fps, respectively. The measured displacement agreed well with analytical model. As shown in Fig. 11b, optically measured displacement increased with time with no obvious lag when the loading velocity was 226  $\mu\text{m}/\text{s}$ . When the loading speed increased to 2.26 mm/s, measured displacement can still reasonably match the model prediction. However, the displacement exhibited large nonlinearity, as discussed in Section 3.2, which would be challenging for high-rate testing at a constant strain rate.

## Discussion

### Loading Velocity and Strain Rate

In this section, the maximum loading velocity and strain rate attainable by the present device are discussed. For this microscopic tensile testing device, it can be seen from Eqs. 9 and 10 that under a ramp force, the strain rate will not be constant either in vacuum or in air because displacement of Sensor B is not absolutely linear. Generally speaking, high strain-rate testing does not necessarily require an absolute constant strain rate, which is indeed very difficult to achieve if possible at all. For example, commercial macroscopic high-rate testing systems can use servohydraulic actuators to reach strain rate up to 500  $\text{s}^{-1}$ , beyond which dynamic testing techniques such as Hopkinson bar technique are used. Open-loop control is used since the actuator moves at such a high velocity that real-time close-loop control is not as effective, which leads to variation from linear displacement profile [38–40]. Therefore it is reasonable to carry out high-rate testing with approximately constant strain rate.

For a given loading velocity, the strain rate would depend on the specimen length. Hence for the generality of the conclusions, loading velocity will be discussed followed with strain rate. To perform a constant-strain-rate test, two requirements should be met: (1) displacement measurement is sufficiently fast such that measured displacement is accurate, and (2) displacement must be linear with time with negligible deviation. The first requirement has been addressed in the preceding section, which resulted in the maximum loading velocities of 45.2  $\mu\text{m}/\text{s}$  and 2.26 mm/s using the capacitive readout and optical measurement, respectively, with the corresponding maximum strain rates of 22.6  $\text{s}^{-1}$  and 1130  $\text{s}^{-1}$  (assuming a typical nanowire sample with gauge length of 2  $\mu\text{m}$ ).

Now let us assess the second requirement. To do so, a term “deviation ratio” is defined as the maximum displacement deviation during the loading normalized by the travel range.

Since the first requirement has been satisfied, the maximum displacement deviation here will be discussed based on the theoretical results. The deviation ratio apparently depends on the travel range (i.e., maximum displacement). For the present device, two travel ranges, 60 and 200 nm, are selected for the purpose of discussion (corresponding to 3% and 10% strain for the gauge length of 2  $\mu\text{m}$ ). For the capacitive readout with the loading velocity of 45.2  $\mu\text{m}/\text{s}$  (Fig. 10b), the deviation ratio is less than 1% for both travel ranges. For the optical measurement with the loading velocity of 2.26 mm/s (Fig. 11c), the deviation ratio is 50% and 15%, respectively. On the other hand, for a given allowable deviation ratio, the maximum displacement deviation can be determined, from which the maximum loading rate  $\xi_{\max}$  and hence the maximum loading velocity and strain rate are obtained. For example, in air, with 10% allowable deviation ratio, the maximum loading velocity is 416  $\mu\text{m}/\text{s}$  and 1.39 mm/s for the travel range of 60 and 200 nm, respectively, with the corresponding maximum strain rates of 208  $\text{s}^{-1}$  and 693  $\text{s}^{-1}$ .

Note that the deviation ratio here is defined based on the deviation from the linear displacement in theory (i.e.  $\frac{\xi t}{k_{SB}}$  in Eq. (9)), which is an overestimate if compared with a fitting line that would also give a constant strain rate. In another way, a straight line is used to fit the displacement curve and the coefficient of determination ( $R^2$ ) is used to assess how linear the displacement is. The  $R^2$  values for linear fitting of two displacement ranges (60 and 200 nm) in both vacuum and air are all over 97%, indicating reasonably good linear fitting. In summary, we have demonstrated the maximum constant strain rate of 22.6  $\text{s}^{-1}$  and 208  $\text{s}^{-1}$  using the capacitive readout and optical measurement, respectively. Note that this is achieved under ramp force (with the actuation voltage up to 15 V in 1 s). In general, the maximum strain rate can be limited by both the actuator and the sensor. Electrostatic actuator can respond very fast, but under ramp force the maximum constant strain rate can be limited by the second requirement mentioned above (displacement linearity) and displacement measurement methods (e.g. imaging and capacitive readout). Applying different actuation voltage profiles (e.g. higher actuation speed or step function), higher constant strain rates can be potentially achieved, at least in air.

To elaborate, an electrostatic actuator can respond generally faster than a thermal actuator, as the bandwidth of the thermal actuator is limited by the heat transfer process (depending on the thermal properties and geometry). The bandwidth of the electrostatic actuator does not depend on the environment (air or vacuum), while that of the thermal actuator does. More specifically, in air the bandwidth is higher because of the heat dissipation to the substrate through air (if there is a substrate immediately below the device). By contrast, in vacuum the heat only dissipates through the anchors at the two ends [41]. However,

relatively fast actuation speed can still be obtained using a thermal actuator especially in air [42].

In addition, the loading velocity and strain rate discussed so far are for the case of no specimen mounted on the device. When a specimen is mounted, the loading velocity and strain rate will decrease. The larger the stiffness of the specimen relative to the stiffness of the device, the more the decrease will be.

## Damping Coefficients

For the present device, the damping force comes from the comb-drive actuator and parallel-plate sensors. For the comb-drive actuator, a laterally driven structure, viscous drag of ambient fluid is the dominant damping source; for the parallel-plate sensor, squeeze film damping is the dominant source [43]. Both damping mechanisms have been studied extensively and here we will briefly discuss them in relation to our device.

Damping coefficient for a comb-drive actuator can be expressed as [44].

$$c_{cd} = \mu \left( \frac{A_{eff}}{d_s} + \frac{A_{eff}}{\delta} + \frac{A_s}{g} + 10.7L \right) \quad (11)$$

where  $\mu$  is the viscosity of air,  $A_{eff}$  is the effective plate area including the areas of the shuttle, fingers and beams,  $A_s$  is the side area of the actuator,  $d_s$  is the distance between the actuator and substrate,  $\delta$  is the effective decay distance, and  $L$  is the characteristic dimension of the moving structure that can be taken as half the width of the shuttle.

The squeeze film damping force on parallel plates can be either elastic force proportional to displacement of the moving plate at a high frequency or viscous force proportional to velocity of the moving plate at a low frequency [45]. The cutoff frequency or frequency at which the two kinds of damping force are equal can be expressed as [45]

$$\omega_c = \frac{\pi^2 g_1^2 p_a}{12\mu w^2} \quad (12)$$

where  $p_a$  is the atmosphere pressure and  $w$  is the width of the plate. For the device reported here, this cutoff frequency is calculated to be 3.7 MHz. Since the device is operated far below this frequency, the viscous damping force dominates while elastic damping force is negligible. In this situation, the damping coefficient for the parallel-plate sensor can be expressed as [45].

$$c_{pp} = \frac{\mu L w^3}{g_1^3} \quad (13)$$

where  $L$  is length of the plate.

Based on these theoretical models, the calculated damping coefficients in air are  $c_A = 3.04 \times 10^{-4}$  kg/s (comb-drive actuator and parallel-plate sensor A) and  $c_B = 2.98 \times 10^{-4}$  kg/s (parallel-plate sensor B), close to the experimentally obtained values in Section 5.1.

## Force Measurement

The capacitive readout AT1006 is used to obtain force and elongation of a specimen on the present device because it is able to measure both sensors' displacements in SEM at the same time. As mentioned in Section 2, when the device is operated for quasi-static testing, force on the specimen equals the force in the load cell, which can be calculated based on the displacements of the two sensors. For high strain rate dynamic testing, force on the specimen equals the force in the load cell minus the damping force and the inertia force of the proof mass. Eq. (5) can be rewritten as

$$F_S = k_S d_B = k_{LC}(d_A - d_B) - c_B d_B - m_B d_B \quad (14)$$

where the first subtracted term is the damping force and the second the inertia force.

The damping force inside SEM environment with a pressure of  $5 \times 10^{-6}$  Torr was studied. In rarefied air, the squeeze film air damping coefficient can be calculated using Veijola's model [46] that replaces the viscosity in Eq. (13) with an "effective" one  $\mu_{eff}$ :

$$\mu_{eff} = \frac{\mu}{1 + 9.658 K_n^{1.159}} \quad (15)$$

where  $K_n$  is Knudsen number that is defined as the mean free path of air molecules divided by the gap distance of the parallel plate. The damping coefficient calculated in this case is on the order of  $10^{-12}$  Kg/s. The damping force is on the order of  $10^{-15}$  N for the largest velocity (45.2  $\mu\text{m/s}$ ) that can be measured by AT1006. Therefore the damping force inside SEM is negligible.

In air, the damping coefficient is on the order of  $10^{-4}$  Kg/s. With the loading velocity of 416  $\mu\text{m/s}$  (strain rate of 208  $\text{s}^{-1}$ ), the damping force is about 40 nN, which can still be neglected when testing specimens like nanowires.

For the inertia force, we only consider it in the vacuum as the upper bound. The acceleration is given by

$$d_B = a_1 \xi (2\pi f_1)^2 \sin(2\pi f_1 t) - a_2 \xi (2\pi f_2)^2 \sin(2\pi f_2 t) \quad (16)$$

$a_1$  and  $a_2$  were calculated to be  $118.6 \times 10^{-9}$  and  $0.52 \times 10^{-9} \text{ m} \cdot \text{s}/\text{N}$  with the known system parameters (e.g.,  $m_A$ ,  $m_B$ ,  $k_{SB}$ ,  $k_{LC}$ ). Even for the maximum loading rate  $\xi = 44.0 \text{ mN/s}$  (corresponding to the maximum loading velocity is 416  $\mu\text{m/s}$  and strain rate of 208/s), the maximum acceleration is  $31.6 \text{ m/s}^2$ , and the maximum inertia force is 0.19  $\mu\text{N}$

(with the mass  $m_B = 5.99 \times 10^{-9}$  kg), which is well below 1% of the force to break a typical nanowire. Moreover, the inertia force oscillates following a sinusoidal form, therefore it at most adds to the noise level without causing a systematic error.

## High-Strain-Rate Testing of Gold Nanowires

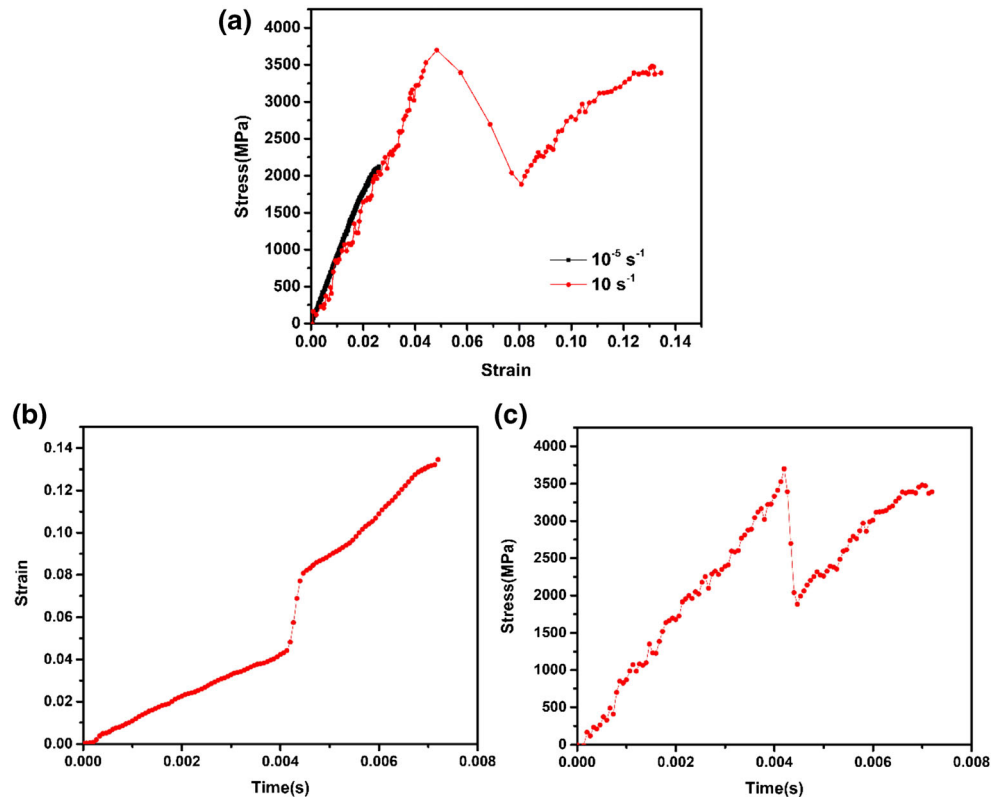
To demonstrate its capability for high strain-rate nanomechanical tensile testing, the device was used to test two single-crystalline gold nanowires at strain rates of  $10^{-5}$  s $^{-1}$  and 10 s $^{-1}$ . The gold nanowires, <110> oriented, were synthesized by physical vapor deposition exhibiting high crystalline quality [47]. The tests were conducted inside SEM and AT1006 was used to measure displacements of the two sensors (A and B), from which the stress and strain were calculated. Nanowires were picked up from a Si substrate using a nanomanipulator (Klocke Nanotechnik, Germany) and clamped on the device by e-beam induced deposition of Pt [8, 24]. The diameters of the two nanowires were 144 nm and 153 nm, respectively. Both the nanomanipulation and the tensile testing were performed inside a SEM-FIB dual beam (FEI Quanta 3D FEG).

Stress-strain curves for the two tested nanowires are shown in Fig. 12a. Young's moduli measured from both tests were around 75 GPa, close to the bulk value. The

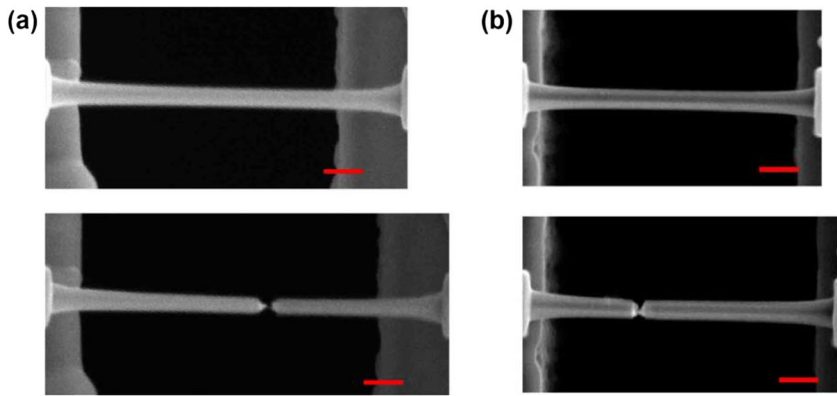
gold nanowire tested at 10 $^{-5}$  s $^{-1}$  exhibited a fracture strength of 2.1 GPa and a fracture strain of 2.8%, indicating brittle fracture. By contrast, the one tested at 10 s $^{-1}$  showed a higher yield strength of 3.7 GPa and a large ductility with the fracture strain of 13.5%. Note a sudden stress drop was captured during the high rate testing. This softening behavior is attributed to the nucleation and propagation of leading partial dislocations from the nanowire surface, which was reported in previous work on FCC metal nanowires [15, 48, 49]. The stress-time and strain-time curves are also shown (Fig. 12b, c). It can be seen that the strain rate was constant until the softening took place. During the softening process, the specimen strain rate increased even though the applied electrostatic load still increased at a constant rate, because the specimen stiffness decreased. The strain rate of 10 s $^{-1}$  was before the softening.

Figure 13 shows the two nanowires before and after testing. By comparing the SEM images, we found that the nanowire tested at high strain rate shows a clear decrease in diameter across the gage length, while the one tested at low strain rate did not show much change in diameter except the necking. It is well known that for metal nanowires plastic deformation starts with surface dislocation nucleation. When two dislocations glide on nonparallel planes inside the crystal, they can form sessile dislocations leading to strain hardening and delayed

**Fig. 12** (a) Stress-strain curves of the two Au nanowires tested at different strain rates. (b, c) Stress-time and strain-time curves for the Au nanowire tested at the strain rate of 10 s $^{-1}$



**Fig. 13** SEM images of the two tested Au nanowires before and after testing. (a) 10/s. (b)  $10^{-5}$ /s. Scale bar: 300 nm



necking. This feature is more prominent as the strain rate increases and the dislocation density increases, which explains why a more uniform decrease in diameter occurs under high strain rates; by contrast, necking occurs at lower strain rates. This observation corroborates the results of Ramachandramoorthy [19] and Tao [50].

## Conclusions

In this paper, we systematically investigated the dynamic response of a MEMS-based nanomechanical testing device in air and in vacuum. The MEMS device consists of an electrostatic actuator, a load cell, and two capacitive displacement sensors. A dynamic model of the device was developed, based on which displacement of sensor B under AC actuation force and ramp actuation force in both air and vacuum were simulated. Both capacitive readout and high-speed optical imaging were used to measure the displacements, which showed good agreement with the modeling results. We have demonstrated the maximum constant strain rate of  $>200\text{ s}^{-1}$  under ramp force. Applying different actuation voltage profiles can potentially lead to higher constant strain rates. However, the capacitive readout used can only measure constant strain rate up to  $22.6\text{ s}^{-1}$  (gauge length  $2\text{ }\mu\text{m}$ ) due to its limited bandwidth, which is nevertheless an order of magnitude higher than the highest strain rate reported so far using an electronic sensor. We demonstrated the device's capability by testing single-crystalline gold nanowires at two strain rates of  $10^{-5}\text{ s}^{-1}$  and  $10\text{ s}^{-1}$ . It was found that increasing strain rate leads to higher yield strength and larger ductility.

**Acknowledgements** The authors gratefully acknowledge financial support from the National Science Foundation (NSF) through Award Nos. DMR-1410475 and CMMI-1929646. The authors would like to thank Dr. T. Fang for providing access to his high-speed camera and Dr. G. Richter for providing the Au nanowire samples.

## Appendix

### Dynamic Response of a Single-Mass-Spring System Under Ramp Force

For a single-mass-spring system as schematically shown in Fig. 14, if the input force is a ramp force  $F(t) = pt$ , the equation of motion can be written as

$$mx + kx = pt \quad (17)$$

Solution to this equation is  $x(t) = \frac{pt}{k} - \frac{p}{k} \sqrt{\frac{m}{k}} \sin\left(\sqrt{\frac{k}{m}} t\right)$ . This solution contains two terms; the first is a ramp term  $\frac{pt}{k} = \frac{F(t)}{k}$ , and the second is a sinusoidal term  $-\frac{p}{k} \sqrt{\frac{m}{k}} \sin\left(\sqrt{\frac{k}{m}} t\right)$ . The sinusoidal term has a frequency  $\sqrt{\frac{k}{m}}$  which is the natural frequency of the system. Its amplitude is proportional to loading rate  $p$  and can be calculated if system parameters  $m$  and  $k$  are known.

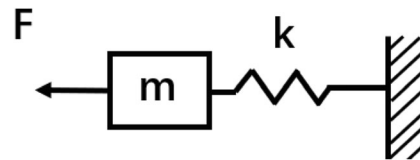


**Fig. 14** Schematic of a single-mass-spring system

### Dynamic Response of a Single-Mass-Spring-Damper System Under Ramp Force

For a single-mass-spring-damper system as schematically shown in Fig. 15, if the input force is a ramp force  $F(t) = pt$ , the equation of motion can be written as

$$mx + cx + kx = pt \quad (18)$$

If the system is an underdamped system, solution to this equation is  $x(t) = \frac{pt}{k} - \frac{cp}{k^2} - \frac{2pm}{k\sqrt{4mk-c^2}} \sin\left(\frac{\sqrt{4mk-c^2}}{2m}t + \theta\right)$ , where

$\theta = \arctan\left(\frac{c\sqrt{4mk-c^2}}{c^2-2km}\right)$ . The solution contains three terms; the first is a ramp term  $\frac{pt}{k} = \frac{F(t)}{k}$ , the second is a constant  $-\frac{cp}{k^2}$ , and the third is a sinusoidal term  $-\frac{2pm}{k\sqrt{4mk-c^2}} \sin\left(\frac{\sqrt{4mk-c^2}}{2m}t + \theta\right)$ . The sinusoidal term has a frequency  $\frac{\sqrt{4mk-c^2}}{2m}$ , which is the damped natural frequency of the system.

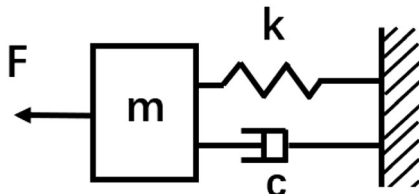


**Fig. 15** Schematic of a single-mass-spring-damper system

## References

- Yao S, Zhu Y (2015) Nanomaterial-enabled stretchable conductors: strategies, materials and devices. *Adv Mater* 27(9):1480–1511
- Yao S, Swetha P, Zhu Y (2018) Nanomaterial-enabled wearable sensors for healthcare. *Adv Healthcare Mater* 7(1):1700889
- Gong S, Cheng W (2017) One-dimensional nanomaterials for soft electronics. *Adv Electron Mater* 3(3):1600314
- Zhu Y, Ke C, Espinosa H (2007) Experimental techniques for the mechanical characterization of one-dimensional nanostructures. *Exp Mech* 47(1):7
- Park HS, Cai W, Espinosa HD, Huang H (2009) Mechanics of crystalline nanowires. *MRS Bull* 34(3):178–183
- Zhu Y (2017) Mechanics of crystalline nanowires: an experimental perspective. *Appl Mech Rev* 69(1):010802
- Zhu T, Li J, Ogata S, Yip S (2009) Mechanics of ultra-strength materials. *MRS Bull* 34(3):167–172
- Cheng G, Chang T-H, Qin Q, Huang H, Zhu Y (2014) Mechanical properties of silicon carbide nanowires: effect of size-dependent defect density. *Nano Lett* 14(2):754–758
- Richter G, Hillerich K, Gianola DS, Monig R, Kraft O, Volkert CA (2009) Ultrahigh strength single crystalline nanowhiskers grown by physical vapor deposition. *Nano Lett* 9(8):3048–3052
- Xu F, Qin Q, Mishra A, Gu Y, Zhu Y (2010) Mechanical properties of ZnO nanowires under different loading modes. *Nano Res* 3(4):271–280
- Agrawal R, Peng B, Gdoutos EE, Espinosa HD (2008) Elasticity size effects in ZnO nanowires— a combined experimental-computational approach. *Nano Lett* 8(11):3668–3674
- Zhu Y, Qin Q, Xu F, Fan F, Ding Y, Zhang T, Wiley BJ, Wang ZL (2012) Size effects on elasticity, yielding, and fracture of silver nanowires: in situ experiments. *Phys Rev B* 85(4):045443
- Zhu T, Li J, Samanta A, Leach A, Gall K (2008) Temperature and strain-rate dependence of surface dislocation nucleation. *Phys Rev Lett* 100:025502
- Chen LY, He M-r, Shin J, Richter G, Gianola DS (2015) Measuring surface dislocation nucleation in defect-scarce nanostructures. *Nat Mater* 14(7):707–713
- Qin Q, Yin S, Cheng G, Li X, Chang T-H, Richter G, Zhu Y, Gao H (2015) Recoverable plasticity in penta-twinned metallic nanowires governed by dislocation nucleation and retraction. *Nat Commun* 6:5983
- Zhong L, Sansoz F, He Y, Wang C, Zhang Z, Mao SX (2017) Slip-activated surface creep with room-temperature super-elongation in metallic nanocrystals. *Nat Mater* 16(4):439
- Bernal RA, Aghaei A, Lee S, Ryu S, Sohn K, Huang J, Cai W, Espinosa H (2014) Intrinsic Bauschinger effect and recoverable plasticity in pentatwinned silver nanowires tested in tension. *Nano Lett* 15(1):139–146
- Chang T-H, Zhu Y (2013) A microelectromechanical system for thermomechanical testing of nanostructures. *Appl Phys Lett* 103(26):263114
- Ramachandramoorthy R, Gao W, Bernal R, Espinosa H (2015) High strain rate tensile testing of silver nanowires: rate-dependent brittle-to-ductile transition. *Nano Lett* 16(1):255–263
- Cheng G, Miao C, Qin Q, Li J, Xu F, Haftbaradaran H, Dickey EC, Gao H, Zhu Y (2015) Large anelasticity and associated energy dissipation in single-crystalline nanowires. *Nat Nanotechnol* 10(8):687–691
- Peng C, Zhong Y, Lu Y, Narayanan S, Zhu T, Lou J (2013) Strain rate dependent mechanical properties in single crystal nickel nanowires. *Appl Phys Lett* 102(8):083102
- Zhu Y, Chang T-H (2015) A review of microelectromechanical systems for nanoscale mechanical characterization. *J Micromech Microeng* 25(9):093001
- Haque M, Saif M (2002) In-situ tensile testing of nano-scale specimens in SEM and TEM. *Exp Mech* 42(1):123–128
- Zhu Y, Espinosa HD (2005) An electromechanical material testing system for in situ electron microscopy and applications. *Proc Natl Acad Sci* 102(41):14503–14508
- Kang W, Saif MTA (2011) A novel SiC MEMS apparatus for in situ uniaxial testing of micro/nanomaterials at high temperature. *J Micromech Microeng* 21(10):105017
- Naraghi M, Kolluru PV, Chasiotis I (2014) Time and strain rate dependent mechanical behavior of individual polymeric nanofibers. *J Mech Phys Solids* 62:257–275
- Naraghi M, Chasiotis I, Kahn H, Wen Y, Dzenis Y (2007) Novel method for mechanical characterization of polymeric nanofibers. *Rev Sci Instrum* 78(8):085108
- Tsuchiya T, Ura Y, Sugano K, Tabata O (2012) Electrostatic tensile testing device with nanonewton and nanometer resolution and its application to C<sub>60</sub> nanowire testing. *J Microelectromech Syst* 21(3):523–529
- Zhu Y, Corigliano A, Espinosa HD (2006) A thermal actuator for nanoscale in situ microscopy testing: design and characterization. *J Micromech Microeng* 16(2):242
- Guan C, Zhu Y (2010) An electrothermal microactuator with Z-shaped beams. *J Micromech Microeng* 20(8):085014
- Naraghi M, Chasiotis I (2009) Optimization of comb-driven devices for mechanical testing of polymeric nanofibers subjected to large deformations. *J Microelectromech Syst* 18(5):1032–1046
- Zhu Y, Moldovan N, Espinosa HD (2005) A microelectromechanical load sensor for in situ electron and x-ray microscopy tensile testing of nanostructures. *Appl Phys Lett* 86(1):013506
- Pantano MF, Bernal RA, Pagnotta L, Espinosa HD (2015) Multiphysics design and implementation of a microsystem for displacement-controlled tensile testing of nanomaterials. *Meccanica* 50(2):549–560
- Erismis MA (2013) Design and modeling of a new robust multi-mass coupled-resonator family with dynamic motion amplification. *Microsyst Technol* 19(8):1105–1110
- Yamahata C, Sarajlic E, Krijnen GJ, Gijs MA (2010) Subnanometer translation of microelectromechanical systems measured by discrete Fourier analysis of CCD images. *J Microelectromech Syst* 19(5):1273–1275
- King H, Warnat S, Hubbard T (2015) Effect of image degradation on nm-scale MEMS FFT optical displacement measurements. In:

- Electrical and Computer Engineering (CCECE), 2015 IEEE 28th Canadian Conference on. IEEE, pp 1387–1392
- 37. Ellerington N, Bschaden B, Hubbard T, Kujath M (2012) Fourier analysis of blurred images for the measurement of the in-plane dynamics of MEMS. *J Micromech Microeng* 22(3):035019
  - 38. Boyce BL, Crenshaw TB (2005) Servohydraulic methods for mechanical testing in the sub-Hopkinson rate regime up to strain rates of 500 1/s. *Sandia Natl Lab Rep*:1–16
  - 39. Zhu D, Rajan S, Mobasher B, Peled A, Mignolet M (2011) Modal analysis of a servo-hydraulic high speed machine and its application to dynamic tensile testing at an intermediate strain rate. *Exp Mech* 51(8):1347–1363
  - 40. de Andrade SF, Zhu D, Mobasher B, Soranakom C, Toledo Filho RD (2010) High speed tensile behavior of sisal fiber cement composites. *Mater Sci Eng A* 527(3):544–552
  - 41. Lott CD, McLain TW, Harb JN, Howell LL (2002) Modeling the thermal behavior of a surface-micromachined linear-displacement thermomechanical microactuator. *Sensors Actuators A Phys* 101(1–2):239–250
  - 42. Shroff SS, Boer MP (2015) Constant velocity high force microactuator for stick-slip testing of micromachined interfaces. *J Microelectromech Syst* 24(6):1868–1877
  - 43. Zhang X, Tang WC (1994) Viscous air damping in laterally driven microresonators. In: *Micro Electro Mechanical Systems, 1994, MEMS'94, Proceedings, IEEE Workshop on*. IEEE, pp 199–204
  - 44. Bao M (2005) Analysis and design principles of MEMS devices. Elsevier, Amsterdam
  - 45. Bao M, Yang H (2007) Squeeze film air damping in MEMS. *Sensors Actuators A Phys* 136(1):3–27
  - 46. Veijola T, Kuusima H, Lahdenperä J, Ryhänen T (1995) Equivalent-circuit model of the squeezed gas film in a silicon accelerometer. *Sensors Actuators A Phys* 48(3):239–248
  - 47. Sedlmayr A, Bitzek E, Gianola DS, Richter G, Möning R, Kraft O (2012) Existence of two twinning-mediated plastic deformation modes in Au nanowiskers. *Acta Mater* 60(9):3985–3993
  - 48. Park HS, Zimmerman JA (2005) Modeling inelasticity and failure in gold nanowires. *Phys Rev B* 72(5):054106
  - 49. Cheng G, Yin S, Chang T, Richter G, Gao H, Zhu Y (2017) Anomalous tensile detwinning in twinned nanowires. *Phys Rev Lett* 119(25):256101
  - 50. Tao W, Cao P, Park HS (2018) Atomistic simulation of the rate-dependent ductile-to-brittle failure transition in bicrystalline metal nanowires. *Nano Lett* 18(2):1296–1304

**Publisher's Note** Springer Nature remains neutral with regard to jurisdictional claims in published maps and institutional affiliations.